POLITECNICO DI TORINO
Repository ISTITUZIONALE

Enhancing additive manufacturing quality and productivity using machine learning: a study on laser powder bed fusion of AISI 316L-2.5%Cu

Original
Enhancing additive manufacturing quality and productivity using machine learning: a study on laser powder bed fusion of AISI 316L-2.5%Cu / Moradi, A., Tajalli, S., Taghian, M., Behjat, A., Saboori, A., Iuliano, L.. - In: PROGRESS IN ADDITIVE MANUFACTURING. - ISSN 2363-9512. - 11:2(2026), pp. 1969-1987. [10.1007/s40964-025-01452-3]

Availability:
This version is available at: 11583/3013038 since: 2026-07-13T14:15:42Z

Publisher:
Springer Nature

Published
DOI:10.1007/s40964-025-01452-3

Terms of use:

This article is made available under terms and conditions as specified in the corresponding bibliographic description in the repository

Publisher copyright

(Article begins on next page)

21 November 2026

Progress in Additive Manufacturing (2026) 11:1969–1987
https://doi.org/10.1007/s40964-025-01452-3

RESEARCH

Enhancing additive manufacturing quality and productivity using machine learning: a study on laser powder bed fusion of AISI 316L-2.5%Cu

Alireza Moradi[1] · Sanae Tajalli[1] · Mohammad Taghian[1] · Amir Behjat[1] · Abdollah Saboori[1] · Luca Iuliano[1]

Received: 23 February 2025 / Accepted: 28 November 2025 / Published online: 5 December 2025
© The Author(s) 2025

Abstract

Metal additive manufacturing (AM) has advanced the fabrication of complex metal components, providing remarkable precision and flexibility in producing different geometries. Integrating artificial intelligence (AI), particularly machine learning (ML), further improves AM by uncovering complex relationships within manufacturing processes and enabling precise quality control. In this study, ML is employed to optimize process parameters in laser powder bed fusion (L-PBF) for AISI 316L-2.5%Cu components, focusing on minimizing defect content and enhancing productivity. Seven supervised ML algorithms, including Bayesian Regression, Decision Tree Regression, Gradient Boosting Regression, Gaussian Process Regression, K-Nearest Neighbors Regression, Random Forest Regression, and Support Vector Regression (SVR), were evaluated for their predictive accuracy using relative density as a target metric. Among these, SVR demonstrated the highest accuracy with a Mean Absolute Error (MAE) of 0.601 and a coefficient of determination (R^2) of 0.842. The optimized process parameters—laser power of 200–250 W, scan speed of 800 mm/s, and hatch distance of 0.13 mm—achieved a relative density exceeding 99.5% while maintaining high productivity. The optimized parameters derived from this approach provide a robust framework for balancing quality, productivity, and defect minimization in AM processes.

Keywords Additive manufacturing · Laser powder bed fusion · AISI 316L · Process optimization · Machine learning

Abbreviations

AM	Additive manufacturing
L-PBF	Laser powder bed fusion
EB-PBF	Electron beam powder bed fusion
ML	Machine learning
PBF	Powder bed fusion
SLM	Selective laser melting
KNN	K-nearest neighbors
DTR	Decision tree regression
SVR	Support vector regression
CAD	Computer-aided design
GPR	Gaussian process regression
VED	Volumetric energy density
RFR	Random forest regression
GBR	Gradient boosting regression
GPR	Gaussian process regression
IN939	Inconel 939
MAE	Mean absolute error
MSE	Mean squared error
SEM	Scanning electron microscope
R^2	Coefficient of determination

✉ Abdollah Saboori
abdollah.saboori@polito.it

Alireza Moradi
alireza.moradighasemabadi@studenti.polito.it

Sanae Tajalli
s314115@studenti.polito.it

Mohammad Taghian
mohammad.taghian@polito.it

Amir Behjat
amir.behjat@polito.it

Luca Iuliano
luca.iuliano@polito.it

[1] Polytechnic University of Turin, Turin, Italy

1 Introduction

Additive manufacturing (AM) is an advanced manufacturing approach that enables the production of complex-shaped parts directly from a computer-aided design (CAD) file in a layer-by-layer manner [1, 2]. AM enhances design flexibility and allows the processing various materials, including polymers, metals, ceramics, and composites [3]. In contrast to traditional manufacturing methods, AM offers significant benefits, including improved material utilization efficiency and the ability to produce near-net-shape structures [4, 5]. Electron beam powder bed fusion (EB-PBF) and laser powder bed fusion (L-PBF) are advanced powder bed fusion AM techniques. In L-PBF, also known as Selective Laser Melting (SLM), high-power lasers selectively melt thin layers of powder according to the CAD file [6].

In contrast, EB-PBF uses an electron beam to melt specific regions of partially sintered powder at elevated temperatures, resulting in distinct microstructures. When carefully optimized process parameters, both techniques can yield exceptional mechanical properties [7–9]. Although the L-PBF process has proven effective in the rapid manufacturing of complex components, its potential applications are limited by challenges such as residual defects [10], surface roughness [11], tensile residual stresses [12], and anisotropic structures [13–15]. However, these challenges can be mitigated by optimizing process parameters to achieve the desired quality of the L-PBF-produced components [14]. Optimizing process parameters requires a multi-objective approach. Achieving this goal necessitates a detailed investigation of all critical parameters and their influence on the surface quality, defect content, microstructure, and mechanical properties of the as-built components. Although more than 130 distinct process parameters have been identified as influencing the L-PBF process [16], key factors such as laser power, laser scanning speed, hatch spacing, and layer thickness are recognized as the most effective hyperparameters impacting the characteristics of the printed structures [17, 18].

Research on the impact of process parameters on L-PBF is crucial for improving component quality and performance. Scholars have conducted extensive studies examining how these parameters influence the microstructure [19], mechanical properties [20], surface quality [21], and electrochemical behavior [22] of components produced by L-PBF. For instance, Saboori et al. [23] investigated the effect of process parameters on the densification and microstructure of Inconel 939 (IN939) alloy. Despite its superior performance, IN939 is prone to cracking due to poor weldability during the L-PBF process. They modified the scanning speed and hatching distance with constant laser power and layer thickness. The research identified specific process parameters that minimize residual porosity and cracking, resulting in nearly pore-free and crack-free samples. In another study, Zhang et al. [24] observed that an increase in laser power leads to an increase in grain size, whereas the scanning speed results in finer grains. Ziri et al. [25] examined the combined influence of powder properties and process parameters on the density of L-PBF-produced 316L stainless steel parts. They measured powder characteristics before producing samples with varying laser power, scan velocity, and layer thickness. Their analysis revealed that powder size significantly affected porosity and defect formation. Powders with higher relative density and better flowability provided wider operating windows, while finer and coarser powders exhibited narrower windows.

Identifying optimal process parameters through trial and error poses significant challenges for engineers. In addition, complex and non-linear relationships between process parameters and performance make it difficult to define them directly. Researchers have applied machine learning (ML) models to find the optimized process parameters range to achieve the desired quality of a part without using excessive time and labor. For instance, Liu et al. [26] applied Gaussian process regression model to optimize the L-PBF parameters for AlSi10Mg. To explain the property variations among specimens with similar grain-scale microstructures, they proposed two new quantitative descriptors, the dimensional scale index and the shape index, which capture differences in sub-grain cell size and boundary morphology. These findings highlighted that fine-scale cellular features, rather than just grain structure, improve the mechanical performance of AlSi10Mg produced by L-PBF, demonstrating the ML models for process design in AM. Moreover, Tapia et al. [27] used Gaussian process regression to model porosity in metallic components fabricated with L-PBF. Their methodology used Bayesian inference to estimate the statistical parameters of the model, while the Kriging method was employed to interpolate porosity values across varying process conditions. The predictive capability of the model was validated experimentally using 17–4 PH stainless steel specimens produced on a ProX 100 system. They demonstrated that their approach can accurately predict porosity and thus inform the selection of process parameters to achieve high relative density in L-PBF parts.

Silbernagel et al. [28] utilized ML techniques to optimize process parameters for L-PBF of pure copper by integrating optical imaging with ML-driven analysis. Optical images were collected and refined using ML algorithms, revealing that optimal track outcomes were achieved for a hatch distance of 50 µm and laser scan speeds of 250–1250 mm/s. Abele et al. [29] also examined the application of L-PBF in producing thin-walled components with controlled porosity and tailored mechanical properties through process

parameter optimization. Their study assessed the impact of laser power, scan speed, and hatch distance on porosity, permeability, pore size distribution, and tensile strength. They customized material attributes using regression models, identifying a single dominant pore size. The findings showed that reducing scan velocity from 1350 to 1150 mm/s decreased porosity and improved tensile strength. Conversely, raising the hatch distance from 0.12 to 0.19 mm led to increased porosity and a loss in strength. Moradi et al. [30] reviewed the range of process parameters across various AM methods, including L-PBF, Directed Energy Deposition (DED), and EB-PBF. They provided detailed data on the parameter ranges, as depicted in Fig. 1, offering valuable insights into optimizing AM processes.

These studies showed that process parameters play a critical role in determining porosity content, dimensional accuracy, and productivity. ML techniques offer a reliable alternative to challenging experiments for optimizing these parameters. ML with high trials speeds up process parameter optimization and decreases experimentation and testing expenses. ML algorithms can learn from datasets and make predictions, unlike physical models. ML techniques like supervised learning use classified information split into training and testing sets to apply models that create correlations between features and the target variable. Supervised learning can further be categorized into two types: regression, which predicts continuous quantities, and classification, which involves predicting discrete class labels [31, 32]. Regression models were used because the target variable (relative density) is continuous in this research.

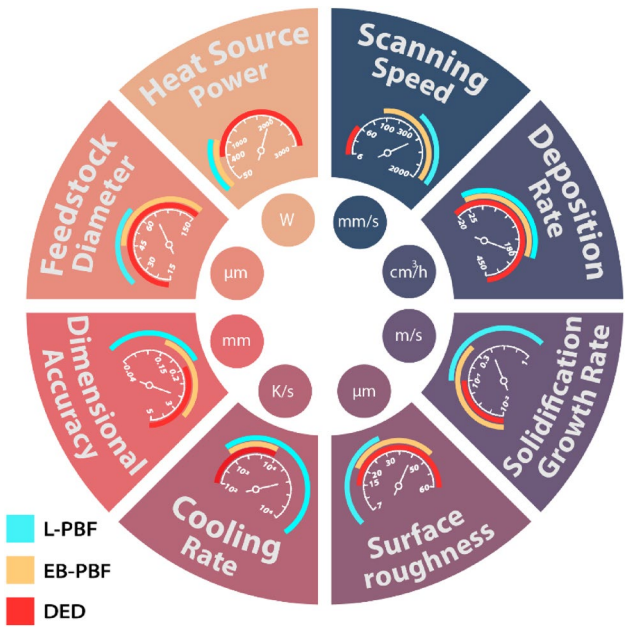


Fig. 1 Different process parameters range for various AM methods [30]

This study evaluates the accuracy of seven supervised learning algorithms including Bayesian regression (BR), decision tree regression (DTR), gradient boosting regression (GBR), Gaussian process regression (GPR), K-nearest neighbors regression (KNN), random forest regression (RFR), and support vector regression (SVR), in predicting the relation between process parameters and defect content in AISI 316L-Cu specimens manufactured by L-PBF using different combinations of process parameters, including laser power, scanning speed, and hatch distance with a constant layer thickness. Employing these seven algorithms was based on their proven effectiveness in previous studies [33–40] for optimizing process parameters in AM processes. These models provide a balance between computational time and predictive accuracy, making them suitable for analyzing the complex relationships between process parameters and defect content. While more complex techniques, such as neural networks, could be explored, this study focuses on models that have consistently demonstrated reliability in comparable contexts, ensuring that the results are both dependable and interpretable. This choice is further justified by the relatively small dataset size in this study, as neural networks typically require substantially larger datasets to avoid overfitting. However, regression-based methods have been shown to perform reliably with limited experimental data in AM [41]. The selection of AISI 316L stainless steel with copper addition was determined by improving its antibacterial characteristics while maintaining its biocompatibility, making it appropriate for biomedical applications like implants. The antibacterial characteristics of this alloy are investigated by Behjat et al. [42], which demonstrates in-situ alloying with Cu enhances antimicrobial activity against Escherichia coli and Staphylococcus aureus while maintaining the overall microstructural integrity. In our study, 2.5 wt% Cu was added to AISI 316L to improve its versatility for biomedical applications. Furthermore, advancing materials for AM through in-situ alloying presents novel opportunities for creating cost-effective and efficient materials with customized properties for particular applications. To reduce potential toxicity and environmental issues, the copper level was restricted in 316L to 2.5 wt% based on the threshold for adding Cu since increased amounts may result in detrimental effects [43]. Moreover, the performance of each model was evaluated using the coefficient of determination (R^2), mean absolute error (MAE), and mean squared error (MSE) metrics. While the primary objective is to establish an accurate relationship between process parameters and defect contents, a secondary goal is to validate the most effective ML algorithm for predicting the trends between VED and relative density.

2 Material and methods

2.1 Materials

The materials used were gas-atomized AISI316L stainless steel powder, supplied by Oerlikon, and gas-atomized copper powder from Sandvik Osprey Ltd. The copper and stainless-steel powders were mixed for 16 h in a low-energy ball mill without the presence of milling balls. The ultimate powder mixture consisted of 2.5 wt% Cu. The chemical composition and morphology of the initial powder mixture are presented in Fig. 2 [44].

2.2 Sample fabrication

After careful consideration, 71 experimental data points were selected for a wide range of three process parameters, including laser power (P), laser speed (v), and laser hatch distance (h), which are reported in Appendix. The process parameter selection was made based on statistical models with the machine and a preliminary analysis that has not been reported. As noted in Appendix, the laser power varied between 100 and 340 W, while the scan speed and hatch distance ranged from 400 to 1000 mm/s and from 0.1 to 0.2 mm, respectively. The wide variety of parameters led to a significant variation in an applicable term named volumetric energy density (VED), which quantifies the amount of input energy per unit volume of the powder bed. As mentioned in Eq. 1, VED is widely used to evaluate the porosity content of materials processed with L-PBF [45].

$$VED = \frac{P}{v.h.t} \tag{1}$$

where P, v, and h represent power, scan speed, and hatch distance, respectively. In (1), t also indicates the layer thickness, which was set to 0.03 mm in this study.

After selecting the process parameters, the samples were manufactured using the PrintSharp 250, an L-PBF machine designed for medium-volume applications. Before printing, the build chamber achieved a residual oxygen level below 0.1%. High-purity Argon maintained an inert atmosphere to prevent oxidation. A bidirectional stripe scanning pattern with a 67° rotation between layers was employed. The components manufactured throughout the experiment had dimensions of $8 \times 8 \times 8$ mm^3. Although some samples with significantly high VEDs, such as samples 50, 32, and 16, were expected to fail in collisions with the recoater, no signs of failure were observed. The platform was preheated to a temperature of 80°C before melting to improve the quality of the parts.

2.3 Density measurement

The density of the samples was measured by Archimedes method, due to its consistency across all density levels, surpassing other density measurement methods [46]. However, this method only provides a general outcome and does not give specific details about the location, shape, and size of pores. Moreover, some analyses were conducted on specific samples using an optical microscope and X-ray computed

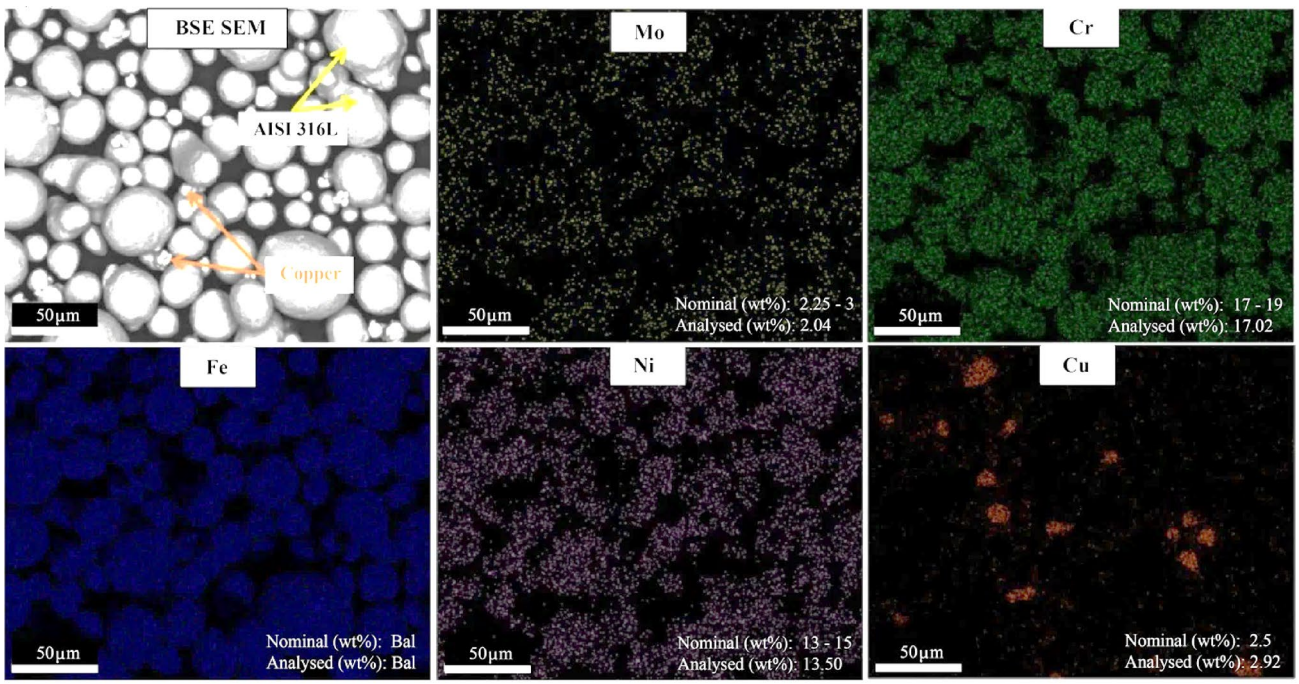


Fig. 2 SEM image of the mixed AISI 316L-2.5% powder with corresponding EDS elemental maps used in this study [44]

tomography based on low, medium, and high VEDs, and the findings will be detailed in the following sections.

Using (2), the apparent density (ρ_a) was determined. Then, the relative density was calculated using (3) with the theoretical density of 7.985 g/cm^3.

$$\rho_a = \frac{W_{dry}}{W_{dry} - W_{inliquid}} \cdot \rho_{liquid} \tag{2}$$

$$\rho_r = \frac{\rho_a}{\rho_t} \tag{3}$$

where W_{dry} is the weight of the specimen in the air in a dry condition, $W_{inliquid}$ is the weight of the specimen after immersion in the liquid, ρ_{ft} is the density of the liquid, which is water in this study, and ρ_t is the theoretical density of the samples. Considering the repeatability of the measurement, the weight of each sample was measured three times in different conditions: dry, immersed in water, and wet after being immersed in water.

2.4 Microstructural and mechanical properties analysis

The microstructure of the selected sample with the highest relative density was analyzed utilizing a Scanning Electron Microscope (SEM, Philips, XL30). Regarding the microhardness of the selected sample, a Vickers indenter with a load of 0.025 kg.f was applied for 15 s on the top surface. Although Five measurements were conducted across various treated zones, their average values will be reported.

2.5 Data preparation for machine learning

Providing a detailed explanation of the process that highlights the importance of each process parameter and identifying the relationship between process parameters and defect content in the manufacturing process is the aim of the framework proposed in this study. As Fig. 3 shows, the process parameters were selected to include a wide range of values for laser power, scanning speed, and hatch distance in the first step. Subsequently, the components were fabricated using a total of 71 specific process parameters, following which their density was measured by the Archimedes method. This comprehensive approach allowed for a thorough exploration of the impact of varying process parameters on the resulting density of the manufactured components. After collecting the density measurement data, the data was split into several sets for testing and training the system. Different sizes of training sets were used in this work to facilitate a more thorough investigation of the data. Afterward, the obtained training dataset is used to train several ML algorithms, each with distinct hyperparameter configurations, to determine the best process parameters to enhance the quality of the component. After model testing, the ML algorithm with the most favorable error metrics was defined in the final stage.

2.6 Machine learning model implementation

This section describes the methodology of the ML approach used to optimize process parameters for L-PBF by establishing an accurate relationship between them and defect content. The dataset was initially split into training (80%) and testing (20%) sets for all seven supervised learning

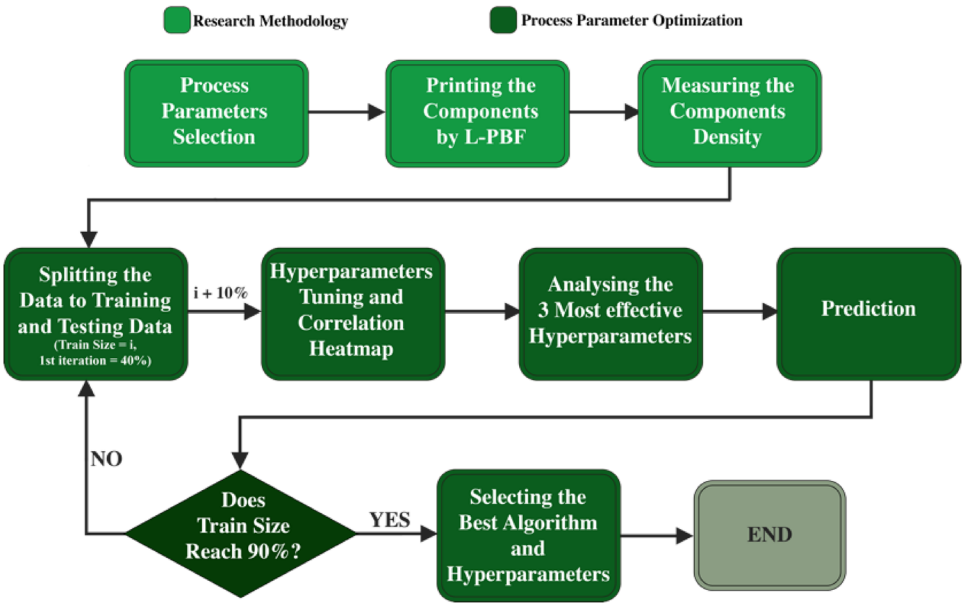


Fig. 3 The proposed framework used in this paper to evaluate the ML models accuracy to predict the relative density of AISI316L-Cu stainless steel samples manufactured by L-PBF

algorithms (BR, DTR, GBR, GPR, KNN, RFR, and SVR). The dataset splitting was performed using the train_test_split function in scikit-learn. Since this function shuffles data based on a random state, we evaluated a wide range of random state values before hyperparameter tuning to ensure that model performance was not dependent on a single data split. The consistent results across these variations confirm the robustness of the reported outcomes. Before training, the input features were pre-processed. For models sensitive to feature scaling (BR, KNN, SVR, and GPR), the features were normalized using the Standard Scaler function in scikit-learn to ensure comparable scales. For tree-based models (DTR, RFR, and GBR), scaling was not required since their performance is unaffected by feature values. Given the significant role of hyperparameters in improving model accuracy, hyperparameter tuning was performed utilizing the Grid Search function.

To avoid excessive computational time caused by defining wide hyperparameter ranges, a preliminary general range was determined to evaluate the impact of each hyperparameter on prediction errors using a correlation heatmap. After completing the correlation heatmap, the three most influential hyperparameters in terms of their effect on prediction accuracy are identified. Following identifying the three most influential hyperparameters, a comprehensive analysis of the top two parameters was performed by plotting prediction errors in 3D, using a wider range with a minor step. Once optimal values for these parameters were identified, the third hyperparameter was similarly analyzed in a 2D plot. The process concluded by selecting the best hyperparameter values to improve model predictions. Moreover, the effect of training data size on model performance was examined by systematically increasing the training set size in 10% increments, from 40 to 90%. This approach investigates the sensitivity of each model to varying train-test data splits.

2.7 Evaluation of machine learning models

Applying a regression model typically requires multiple metrics for a comprehensive evaluation [32]. The accuracy of the chosen models is assessed using three statistical metrics: the R^2, the MAE, and the MSE.

MAE represents the average absolute deviation for each statistic, which indicates prediction accuracy [47]. MAE provides a more accurate representation of the actual amount of the prediction error, in contrast to other error metrics, by adequately addressing the issue of error cancellation [48]. It should be noted that the MAE value is expressed in the same units as the original target variable. This feature facilitates comparisons among multiple ML models, specifically for the target data, rather than across different prediction tasks [32].

MSE denotes the sample standard deviation of the discrepancies between predicted and actual values, used as a metric that calculates the ratio between the squared differences of predicted and actual values and the total number of data points. It is worth noting that the MSE is more sensitive to outliers than the MAE [48, 49].

The coefficient of determination, often denoted as R^2, measures the strength of the relationship between two variables. It assesses the accuracy of the regression equation in fitting the observed data and capturing the variability in the dependent variable. Specifically, R^2 quantifies the level of variation in the target variable that can be assigned to the changes in independent input variables in a regression model. Essentially, it signifies the degree of correlation between the input and target variables [50]. It is essential to note that assessing prediction accuracy using only R^2, especially in non-linear regression, is inadequate. Therefore, in this study, R^2 is not the exclusive statistic for evaluating model performance.

Additionally, R^2 has certain limitations. Although the increase of independent variables results in a rise in R^2, especially in large datasets, a very high value of R^2 may indicate an overfitted model, while an accurate model may have a reduced R^2. Negative R^2 values also suggest that predictions are worse than the mean target value [32]. MAE, MSE, and R^2 can be calculated by (4), (5), and (6).

$$\mathrm{MAE} = \frac{1}{n}\sum_{i=1}^{n}|y_i - \hat{y}_i| \tag{4}$$

$$\mathrm{MSE} = \frac{1}{\mathrm{n}}\sum_{\mathrm{i}=1}^{\mathrm{n}}(\mathrm{y_i} - \widehat{\mathrm{y}}_\mathrm{i})^2 \tag{5}$$

$$R^2 = \frac{\sum_{\mathrm{i}=1}^{\mathrm{n}}(\widehat{\mathrm{y}}_\mathrm{i} - \overline{\mathrm{y}})^2}{\sum_{\mathrm{i}=1}^{\mathrm{n}}(\mathrm{y_i} - \overline{\mathrm{y}})^2} \tag{6}$$

where y_i, $\widehat{y}_i$, $\overline{y}$ represent actual, predicted, and mean value, respectively; n is the total number of data points. The high R^2 value and the low MAE and MSE values suggest that the analysis and statistical model are accurately representative [2].

To address the limitations mentioned earlier and provide a comprehensive analysis of algorithm accuracy, the Index of Merit (IM) is introduced in this study. As shown in (7), IM integrates the three statistical measures (MAE, MSE, and R^2) into a single metric that provides a more holistic view of model accuracy. A value closer to zero indicates optimal predictive performance, whereas values further from zero suggest decreasing accuracy [51, 52].

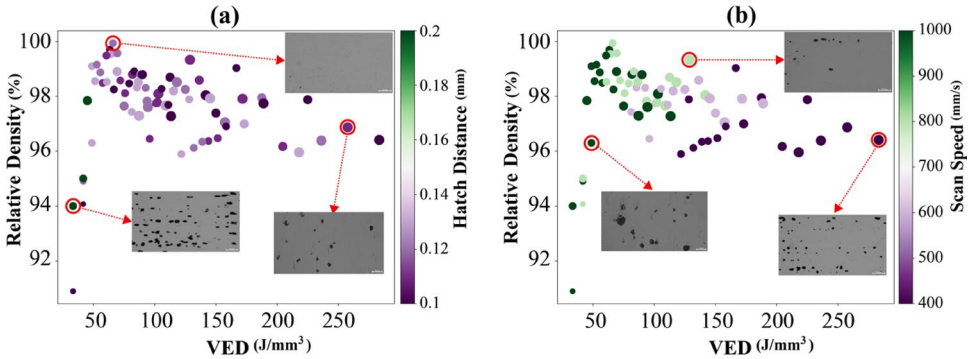


Fig. 4 Illustration of the relationship between the VED and the relative density. The size of the points represents laser power, while color indicates **a** hatch distance and **b** scan speed

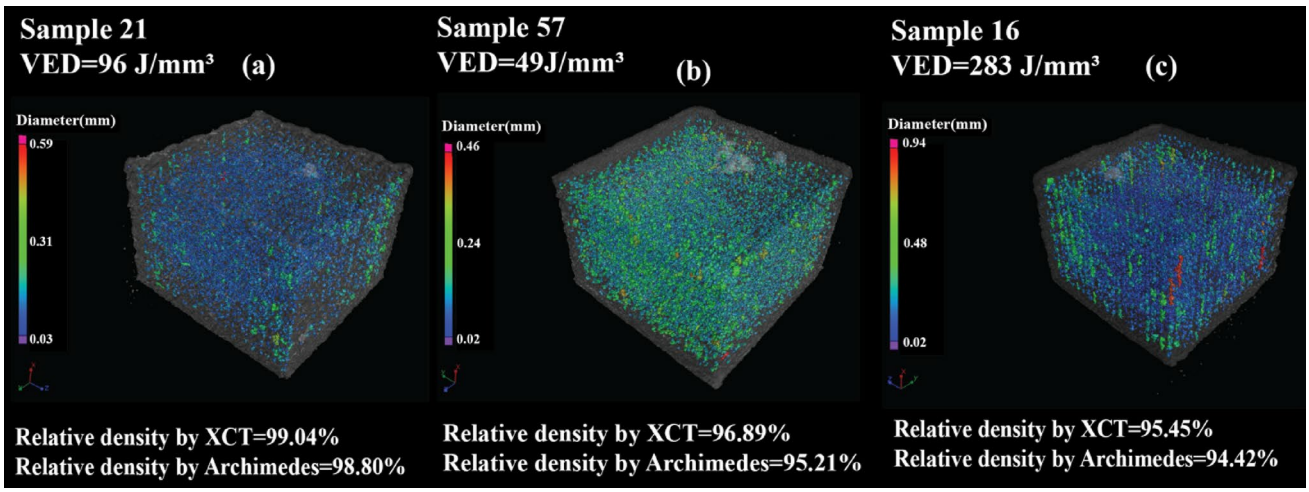


Fig. 5 Relative density of samples at varying VEDs, measured by XCT and Archimedes method

$$IM = \sqrt{(\mathrm{MAE})^2 + \mathrm{MSE} + (1 - \mathrm{R}^2)^2} \tag{7}$$

3 Results and discussion

3.1 Density and process parameters

Figure 4 illustrates the impact of process parameters on the relative density of parts as they vary with the VED. The size of the points shows the laser power, while the hatch distance and scan speed are indicated by the color in Fig. 4a and b, respectively. VED varies from 33 to 283 (J/mm^3), leading to component densities ranging from 90.9 to 99.9%. The VED of 66 J/mm^3 was optimal in this study, achieving the maximum density (99.9%) in Sample 38. Inadequate laser energy at lower VED values results in partial fusion, which reduces the components density.

Nevertheless, if the VED exceeds 50 J/mm^3, the L-PBF process produces components with a high level of density, as confirmed by optical micrographs as shown in Fig. 4. The main microstructural defects in L-PBF include gas-induced porosity (GIP), lack of fusion (LOF), keyhole (KH), and balling. GIP defects are small, spherical, and uniformly distributed, forming due to gas entrapment from high temperatures, gas atomization, laser evaporation, or surface contaminants [53], while LOF defects are irregular, larger, and occur due to insufficient energy, material shrinkage, or oxidation, affecting layer bonding [54, 55]. KH defects result from excessive energy input, creating deep vapor voids due to material evaporation and plasma formation [56]. Balling occurs at high scan speeds or low energy input, leading to bead-like formations due to surface tension instability, worsened by oxides or moisture [57]. In this study, as VED grows, a decrease in density occurs because of GIP formation, which highlights the significance of vaporization effects within the high range of VED. Therefore, both extremely low and extremely high values of VED are generally inappropriate for creating a fully dense component. Thus, as the VED changes, different porosities can be observed.

Three samples (21 Fig. 5a, 57 Fig. 5b, and 16 Fig. 5c) with varying VEDs were analyzed to assess their relative density. Although the Archimedes and XCT approaches showed a similar trend, the relative density measured by the Archimedes method was consistently lower than that obtained by XCT, highlighting the superior ability of XCT to detect internal voids. These findings highlight the important role

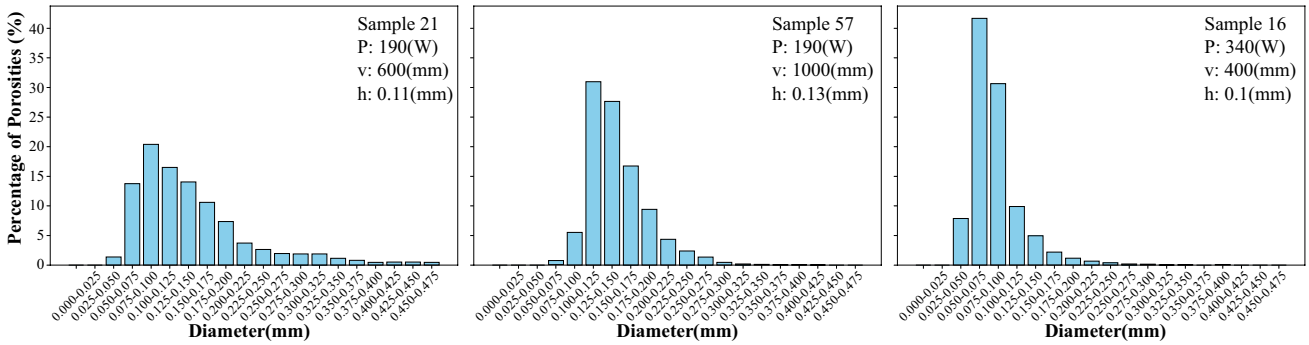


Fig. 6 Illustration of pore diameter distribution for three different samples characterized by XCT

of XCT in precise density measurement and quality control in AM.

Figure 6 presents the pore diameter distribution (in percentage) for three selected samples processed under different VEDs based on XCT data. The distribution illustrates the impact of VED on the dimensions and number of porosities in components produced by L-PBF. Sample 21, with a moderate VED (96 J/mm^3), demonstrates a relatively uniform distribution of porosities, with the majority (over 70%) of pores falling within the 0.05–0.25 mm range. This suggests a stable melt pool and adequate input energy that minimized both GIP and LOF defects. In contrast, Sample 52, fabricated with a low VED (49 J/mm^3), shows a higher concentration of porosities in the higher diameter ranges, with nearly 60% of pores distributed between 0.01 and 0.15 mm. This pattern indicates importance of LOF defects caused by insufficient energy input, which leads to incomplete melting [54, 55]. Sample 16, processed at a high VED (216 J/mm^3), shows a different trend with an increased amount of smaller pores, particularly within the 0.05–0.75 mm range. This distribution is characteristic of GIP, which is typically spherical and results from excessive vaporization and gas entrapment during melting [53].

These findings align with the previously described relationship between VED and defect content. Therefore, controlling the energy input is critical for achieving the higher density and quality of L-PBF samples.

3.2 Hyperparameter tuning

A systematic approach was employed for hyperparameter tuning to enhance the performance of the ML models. Rather than exploring an extensive range of hyperparameters, which can be computationally expensive, shorter ranges were initially defined for almost all hyperparameters of each model based on prior studies. This process significantly reduced computational time while maintaining model accuracy, providing a comprehensive overview of the impact of hyperparameters on model performance.

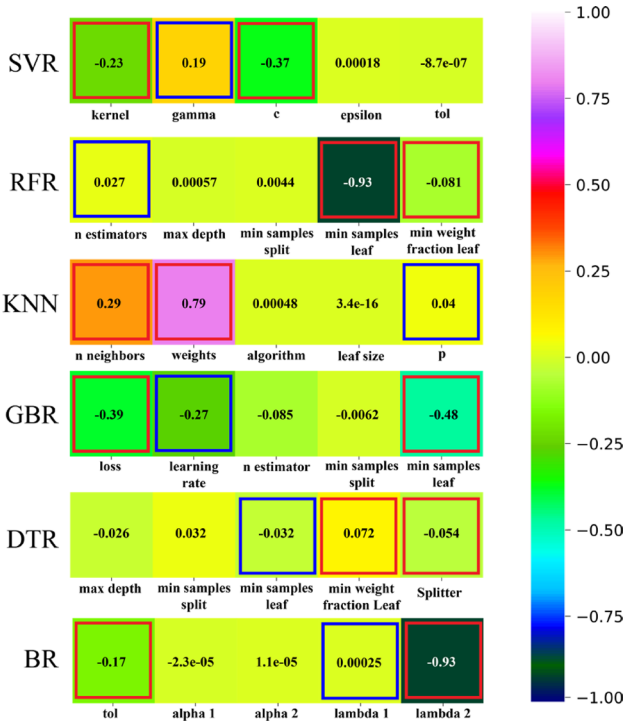


Fig. 7 Correlation heatmap of hyperparameters and R^2 for all algorithms

In this approach, the key hyperparameters with the most significant impact on model accuracy, as indicated by R^2, can be identified. However, it should be noted that if inappropriate ranges for hyperparameters are defined, inaccurate correlation heatmaps may result, potentially leading to the selection of wrong hyperparameter values. This highlights the importance of carefully selecting parameter ranges for reliable tuning outcomes.

A correlation heatmap was generated to visualize the relationship between each hyperparameter and the R^2 score. Figure 7 displays the heatmap showing the relationship between each hyperparameter and the R^2 score, visually representing the correlations between the algorithms and the predictive accuracy. This analysis identified the top three most influential hyperparameters with the highest absolute

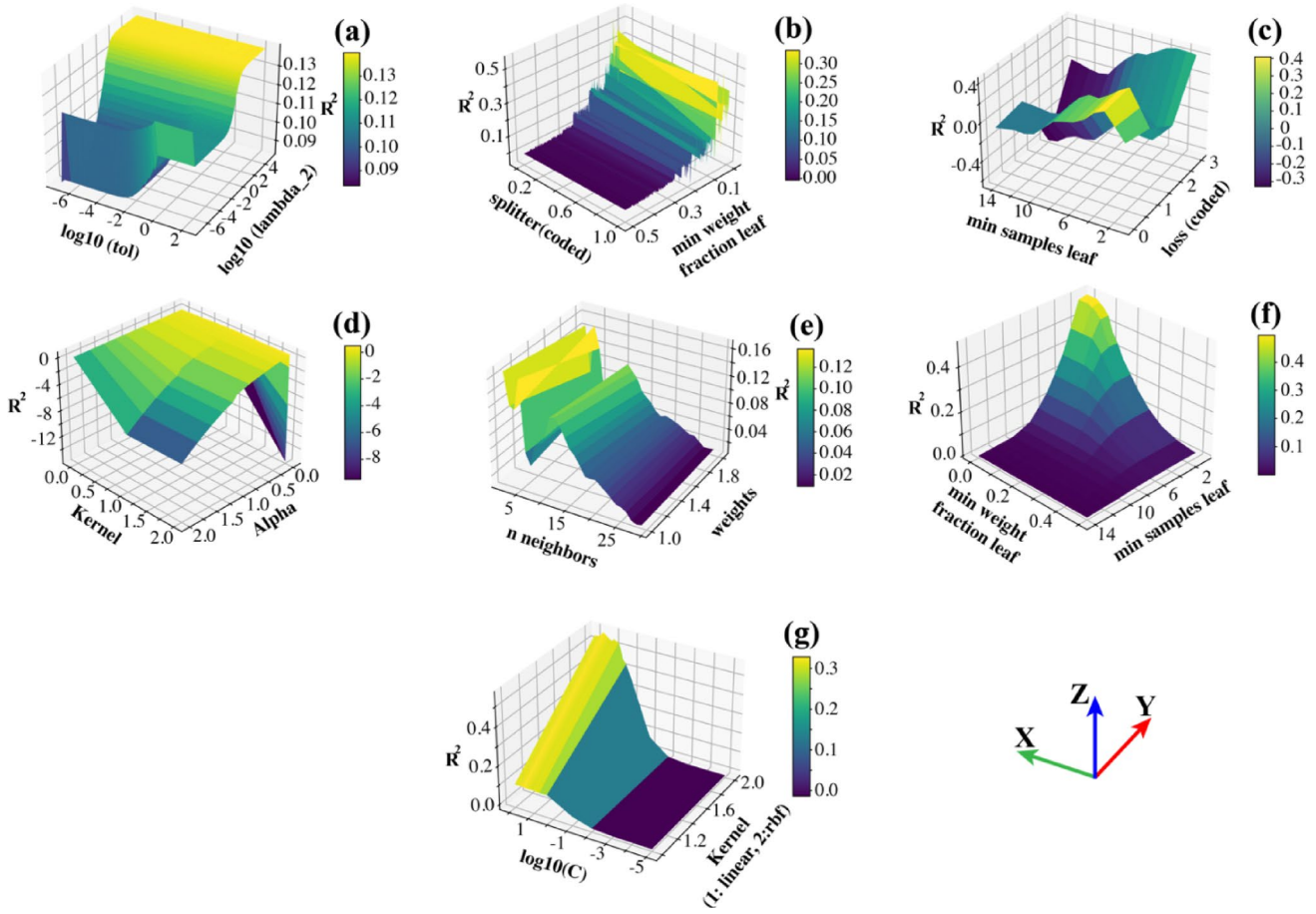


Fig. 8 R^2 surface for the two most effective hyperparameters of all algorithms. **a** BR, **b** DTR, **c** GBR, **d** GPR, **e** KNN, **f** RFR, and **g** SVR

Table 1 The optimized values of the two most effective hyperparameters for all algorithms

	BR	DTR	GBR	GPR	KNN	RFR	SVR
X	Tol:7.74e-4	0.06	Absolute error	2.78e-3	2	1	34
Y	Lambda2: 1.00e+5	best	3	Matern (Length scale = 1, nu = 1.5)	Uniform	0.05	rbf

values in Fig. 7. It is important to note that, in Fig. 7, positive correlations indicate that increasing the hyperparameter enhances accuracy, while negative correlations represent that reducing that specific hyperparameter improves performance. Subsequently, the hyperparameters were evaluated more comprehensively using more comprehensive ranges and smaller step sizes. The GPR model has three primary hyperparameters, excluding it from the heatmap analysis employed for key hyperparameter identification. In the next step, a 3D plot was used to examine the effect of the two most impactful hyperparameters on prediction accuracy, highlighted with red rectangles in Fig. 7, allowing for identifying their optimal values, as shown in Fig. 8 and Table 1.

Once these two parameters were optimized, the third hyperparameter, highlighted with the blue rectangle shown in Fig. 7, is analyzed in a 2D plot to determine its best value, as illustrated in Fig. 9. It is important to note that Fig. 9a–g, represent the R^2 value obtained from BR, DTR, GBR, GPR, KNN, RFR, and SVR, respectively. For example, in the case of the RFR model, parameters such as min_samples_leaf, min_weight_fraction_leaf, and n_estimators, as suggested by the correlation heatmap, were analyzed. After identifying the two most influential hyperparameters, including min_samples_leaf and min_weight_fraction_leaf, as shown in Fig. 8f, a 3D plot was generated to visualize how their interaction affected the R^2 score. The optimal values for these parameters were then fixed, and the third hyperparameter, n_estimators (Fig. 9f), was fine-tuned to enhance the model performance. It is worth noting that Figs. 7, 8, and 9 are related to the analysis of the models using a training size of 50%.

In the SVR model, although the gamma parameter showed a stronger correlation in the heatmap plot (Fig. 7) compared to epsilon, there are only two possible values for

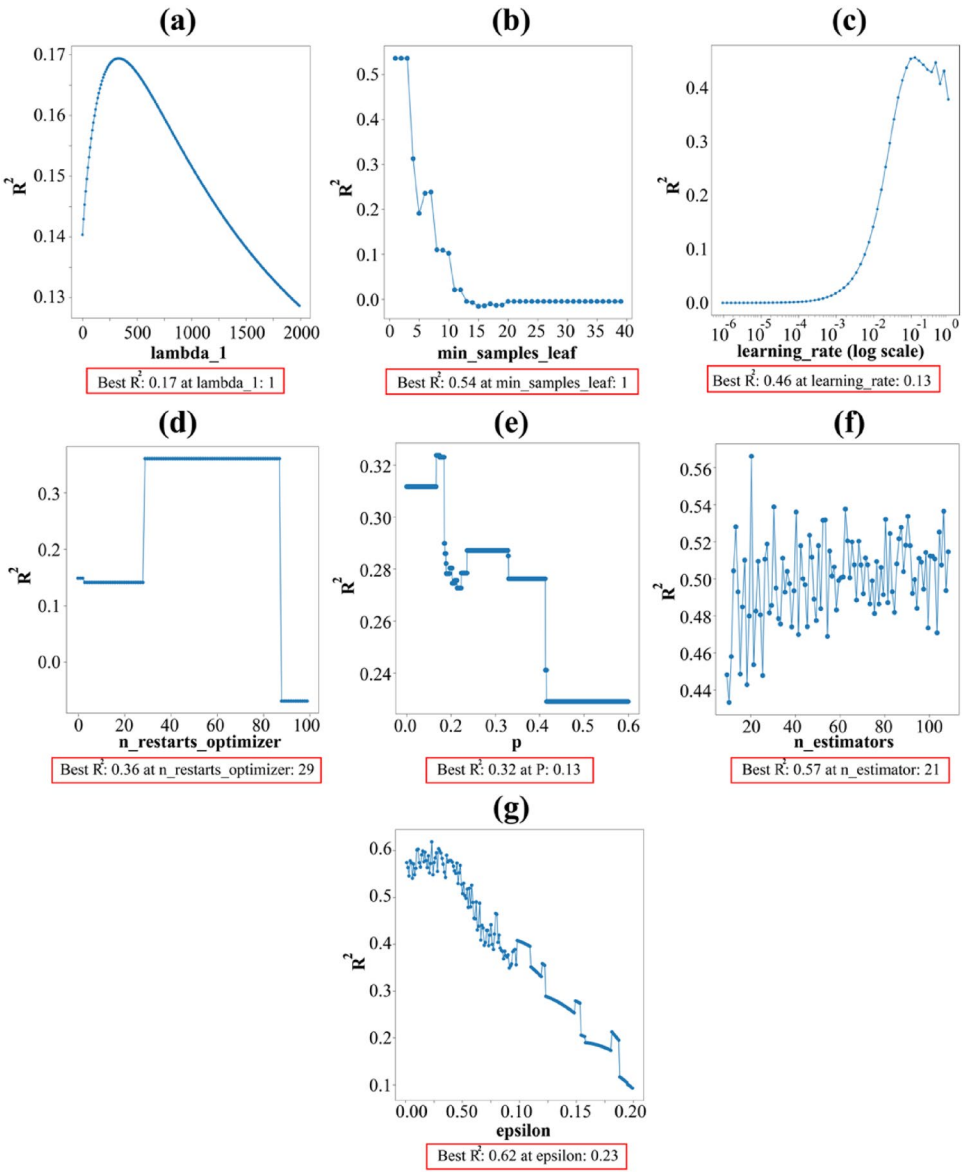


Fig. 9 R^2 chart for the third effective hyperparameters of all algorithms with their optimized value

gamma. As a result, a 2D plot analyzing this hyperparameter would not provide sufficient insight. Consequently, as shown in Fig. 9, the epsilon parameter, the third hyperparameter, was selected for further analysis in the 2D plot due to its more comprehensive range of values. However, both gamma values were tested during tuning to ensure a thorough evaluation. This tuning process significantly improved the prediction accuracy in all models, ensuring that the selected hyperparameters yielded optimal results. The final hyperparameter values were then used in subsequent model evaluations, including comparisons of predicted versus actual values for model validation.

3.3 Training size effect and model performances

After completing the hyperparameter tuning process and selecting the optimized hyperparameters, we used these values in the ML algorithms to predict the target variable (the relative density of the testing data) for which the actual values were already known. At the beginning of the process, based on the statistical models, the main dataset was randomly split into training and testing sets to prevent overfitting caused by carefully selecting data points. Overfitting is a prevalent issue in ML, where a model attains high accuracy on training data but is not very accurate on unseen data. This phenomenon occurs when the model learns noise in the training set rather than identifying the actual relationships within variables in the data [58]. Moreover, the model developed in this study is trained on a large dataset, which

minimizes the likelihood of overfitting [59] and enables evaluation of a wide range of process parameters. The training and testing datasets were applied consistently across all algorithms throughout the process. The efficiency of each model was subsequently assessed by quantifying the differences between the predicted and actual values. The impact of different train sizes on model performance, assessed through R2, MAE, and MSE, is an essential part of model evaluation and optimization. Figure 10 depicts the effect of varying train sizes (40%, 50%, 60%, 70%, 80%, 90%) on the error metrics across several algorithms: BR, DTR, GBR, GPR, KNN, SVR, and RFR. The general trend observed in Fig. 10a indicates that as the training size percentage increases, the MSE generally tends to rise in most algorithms, affecting prediction accuracy. This increase in MSE is more noticeable in the BR. For instance, at the training size of 40%, the BR demonstrates an MSE value of 1.987, which increased to 7.043 by raising the training size to 90%. The significant rise in MSE highlights the model's sensitivity to decreased testing size, leading to lower prediction efficiency. However, some algorithms, such as SVR, demonstrate the inverse trend, where an increase in training size decreases the MSE, indicating enhanced predictive accuracy with larger datasets.

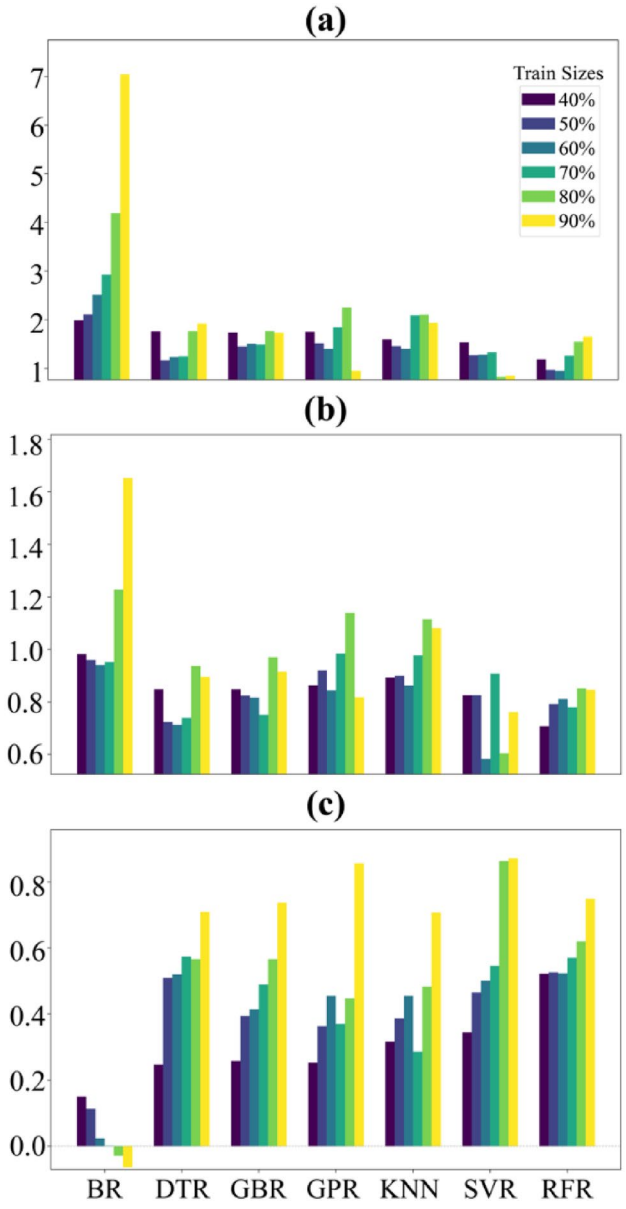


Fig. 10 **a**, **b**, and **c** respectively represent the MSE, MAE, and R^2 values for different values and train sizes of each ML algorithm

The effect of train size on MAE follows a similar pattern to that of MSE, as shown in Fig. 10a and b. The lowest MAE values are typically observed at the 60% training size, while larger training sizes of 90% result in higher MAE values. For example, in the GBR model, the MAE at 60% train size is 0.713, but this value rises to 0.896 at 90%. While this suggests that a 60% train size may yield optimal results for minimizing MAE, it is essential to note that other error metrics, such as MSE and R^2, must also be considered to identify the most appropriate train size for overall model performance.

Figure 10c shows that R^2 increases as the training size rises, indicating improved predictive accuracy. The most significant improvements in R^2 occur when the training size reaches 80% and 90%. For instance, in the GPR model, the R^2 value starts at 0.252 with a 40% training size but more than triples to 0.856 when the training size reaches 90%. Similarly, the SVR model significantly improves, with the R^2 increasing from 0.344 at a 40% train size to 0.842 and 0.871 at 80% and 90%, respectively. However, this trend is not consistent across all algorithms. In the BR, an opposite pattern is observed, where increasing the training size leads to a decrease in R^2, highlighting the distinct behaviour of each algorithm. Although using 90% of the data for training usually results in the highest R^2 score across various algorithms, using only 10% for testing increases MAE and MSE. This shows that considering only R^2 is not enough to evaluate the prediction accuracy of each model, and other error metrics should also be considered.

The IM values in Table 2 indicate that a training size of 80% achieves an optimal balance between three error metrics, depending on the algorithm applied. Among the analyzed algorithms, SVR provides the highest accuracy with the best IM value of 1.13 in almost all training sizes. In contrast, the BR, with the worst IM value of 3.13, displays the lowest prediction efficiency throughout the evaluation. These findings highlight the necessity of choosing a proper training size and optimal hyperparameters to optimize accuracy and error metrics for each algorithm.

Table 2 IM values were calculated for all ML algorithms with different training sizes

	BR	DTR	GBR	GPR	KNN	RFR	SVR
40	1.92	1.78	1.77	1.78	1.72	1.46	1.67
50	1.96	1.46	1.62	1.69	1.65	1.41	1.54
60	2.10	1.48	1.63	1.59	1.60	1.41	1.45
70	2.21	1.47	1.58	1.80	1.89	1.49	1.56
80	2.54	1.70	1.71	1.71	1.87	1.59	1.13
90	3.13	1.70	1.65	1.34	1.76	1.60	1.28

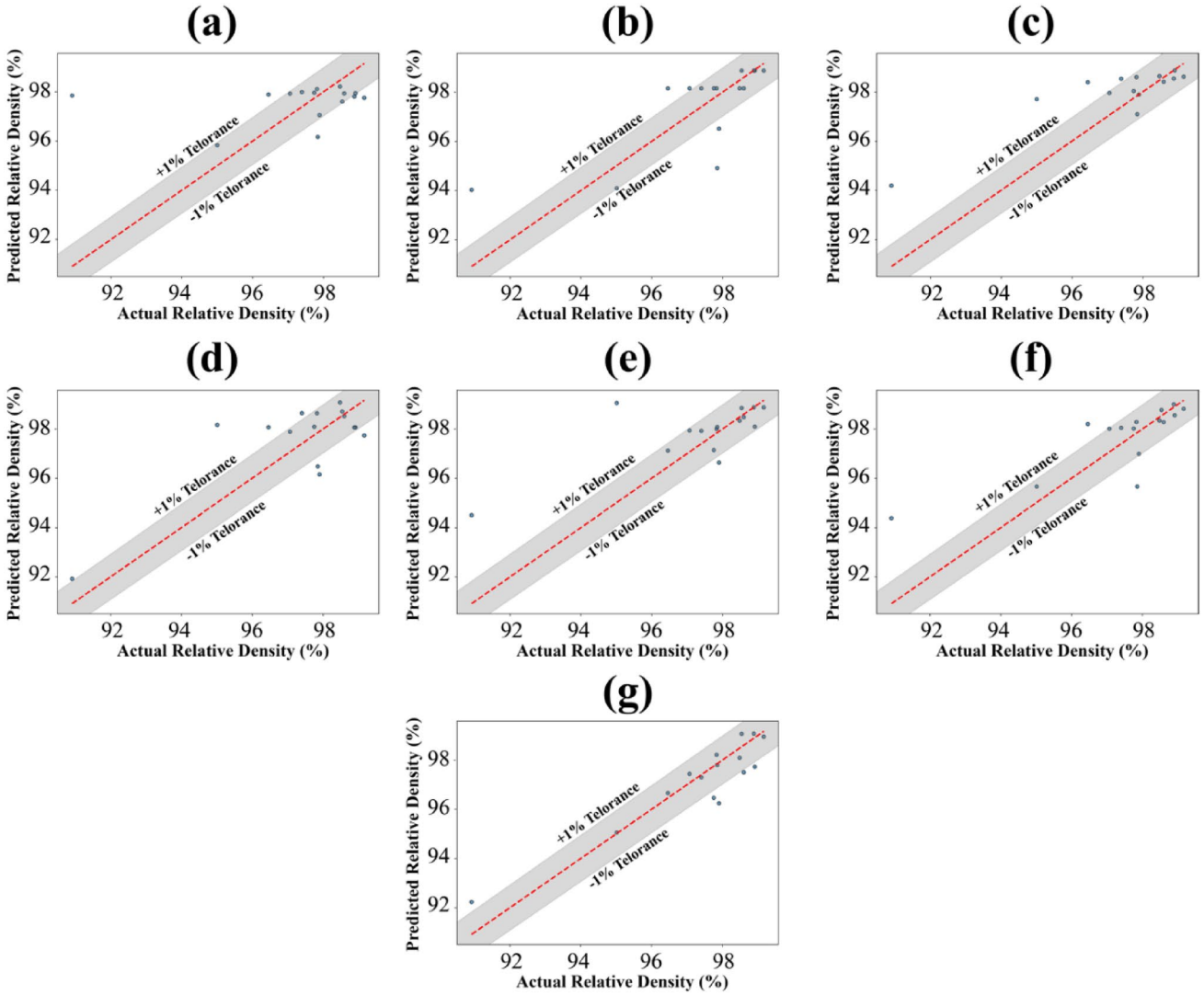


Fig. 11 Comparison of predicted vs. actual relative densities for all algorithms at 80% training size. The red dashed line indicates the optimal prediction (when projected values align with actual values), and the gray-shaded area indicates ± 1% tolerance range

3.4 Prediction accuracy and process parameter optimization

This section evaluates the predictive accuracy of various algorithms by comparing the predicted and actual relative densities on the vertical and horizontal axes, respectively. Figure 11a–g compare the actual and predicted relative densities in AISI 316L-2.5%Cu components manufactured by L-PBF for BR, DTR, GBR, GPR, KNN, RFR, and SVR, respectively, at 80% training size. The proximity of the points to the red dashed line, representing perfect predictions, indicates the accuracy of each model. Most models are less accurate in components with lower relative densities, except for SVR and GPR, which consistently maintain high precision across the entire range. This phenomenon occurs because the dataset primarily contains samples with

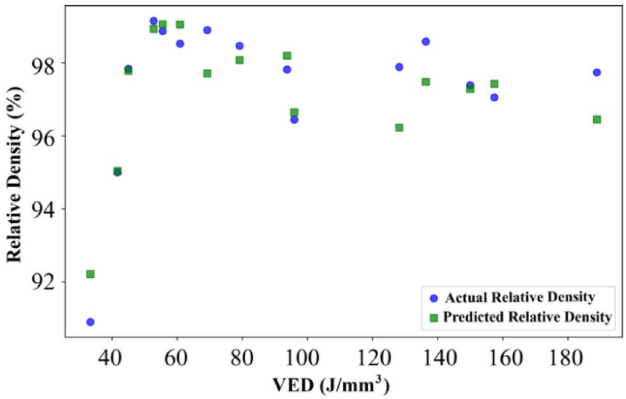


Fig. 12 Comparison of actual and predicted relative density as a function of VED using SVR with optimized hyperparameters at the training size of 80%

relative densities higher than 97%, which limits the ability of models to effectively learn and predict the relative density of components with lower relative density. For components with higher relative density, prediction accuracy improves in all models, as shown by the closer alignment of points with the red line. However, it is important to note that k-fold cross-validation was used for all algorithms to ensure robust model evaluation and avoid overfitting. In a run k-fold cross-validation run, the dataset is randomly shuffled and divided into k folds (In this study, k = 3). Each fold is sequentially used as a test set, while the remaining folds serve as the training set, ensuring that every subset is tested once [60].

Figure 12 compares the actual and predicted relative densities of the best ML model attained using testing data. The SVR algorithm with the optimized hyperparameters (kernel = rbf, C = 215.44, Max_iter = 990, tol = 0.0278, epsilon = 0.1) was applied to predict relative densities at 15 testing points. Among the models, SVR excelled, attaining the lowest MAE of 0.601, MSE of 0.640, and highest R^2 of 0.842 at the training size of 80%. As shown in Fig. 12, the predictions closely match the actual values. Additionally, Fig. 13 highlights the optimal values of the target variable (relative density), the corresponding VED, and the same trend shown in Fig. 4 for manufacturing under optimal conditions.

Furthermore, previous studies [32, 52] have highlighted the predictive efficiency of these algorithms, particularly SVR and RFR. SVR has been recognized for its ability in fast and accurate predictions, especially in high-dimensional data, while RFR offers enhanced model stability and reduced overfitting by compiling the results of multiple tree structures [32]. Similar to these findings, our results also demonstrated that SVR achieved the highest accuracy with relatively low computational cost, further validating its suitability for the task.

Figure 13 illustrates the relationship between relative density and process parameters for four different scan speeds: 400, 600, 800, and 1000 mm/s based on the best predictor model, SVR, at the training size of 80% with specific optimized hyperparameters. These values are within the specified range of hatch distance (0.1–0.2 mm) and power (100–400 W). Generally, as the scan speed increases, the contour plots in Fig. 13 indicate a continuous rise in

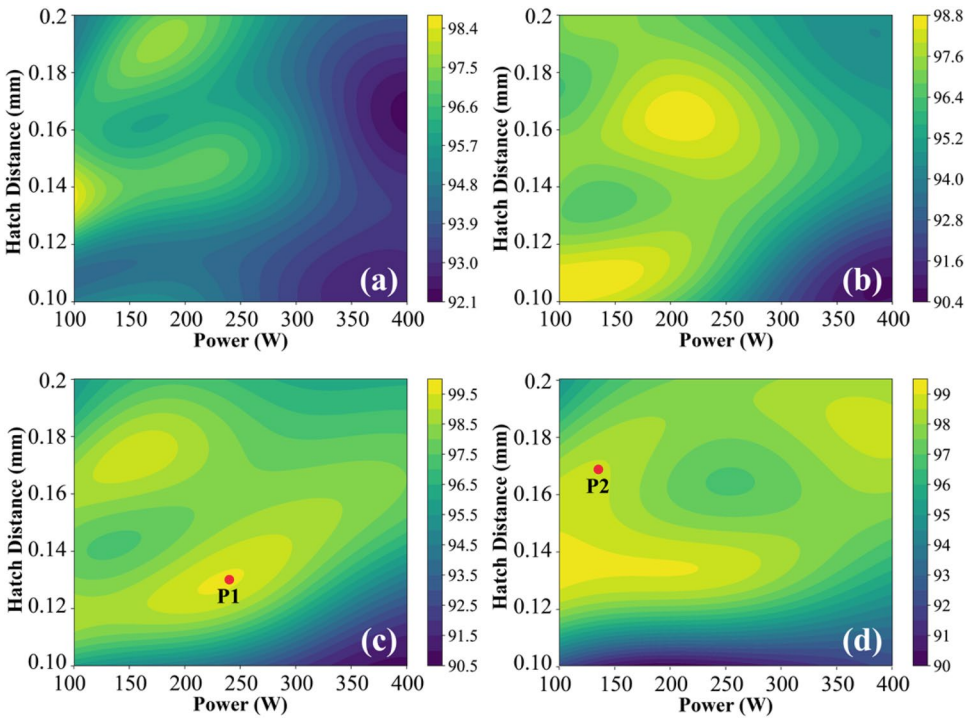


Fig. 13 Predicted relative density (%) for different scan speeds of 400, 600, 800, and 1000 mm/s illustrated in (**a**), (**b**), (**c**), and (**d**), respectively, by varying power (100–400 W) and hatch distance (0.1–0.2 mm) ranges, using the SVR algorithm at the training size of 80% after hyperparameter tuning

predicted relative density, as shown by the expansion of yellow and green regions. This trend highlights the influence of scan speed on the densification process, where higher scanning speeds caused enhanced relative density under the given conditions.

At the scanning speed of 400 mm/s, Fig. 13a, the minimum relative densities are observed in the power range of 300–400 W, independent of the hatch distance. Conversely, the highest relative densities at this scan speed are obtained when the power ranges from 100 to 200 W, with the hatch distance between 0.13 and 0.15 mm. This suggests that optimal relative density at the scan speed of 400 mm/s can be achieved within these specific process parameters at lower power levels combined with moderate hatch distances.

At the scanning speed of 600 mm/s, Fig. 13b, the predicted relative density improved across the entire hatch distance and power range compared to the previous scan speed. However, the maximum predicted relative density is still lower at scanning speeds of 800 and 1000 mm/s. The lowest relative density is observed when the power exceeds 300 W, particularly at hatch distances less than 0.12 mm. On the other hand, when the power is less than 300 W, the highest relative densities are achieved in two specific hatch distance ranges, 0.10–0.11 mm and 0.15–0.18 mm.

The maximum predicted relative density at a scan speed of 800 mm/s, as shown in Fig. 13c, increased by 0.8% compared to the previous scan speed of 600 mm/s and by 1.1% compared to the speed of 400 mm/s, reaching a peak of 99.5%. The highest relative densities were achieved in the hatch distance range of 0.12–0.18 mm. However, at high P values, particularly around 400 W, the highest percentage of porosity would be possible, especially in small hatch distance ranges.

At the scanning speed of 1000 mm/s, Fig. 13d, the maximum relative density decreased by 0.5%. The predicted relative density value reached its lowest value at the hatch distance range of less than 0.12 mm. For hatch distances greater than 0.12 mm, the power should be set between 100 and 250 W to achieve high relative density, particularly at a hatch distance of 0.14 mm.

Figure 13 shows that while high relative density values are achievable in all four plots, a scanning speed of 800 mm/s can be considered optimal. At this scanning speed, porosities can be minimized using a power setting of approximately 250 W and a hatch distance of 0.13 mm. This model can achieve various objectives by analyzing the relationship between process parameters and porosity content, such as maximizing productivity and identifying optimal process parameters for that goal.

In AM, the build rate (BR) quantified in mm^3/s significantly influences fabrication time [61]. An increased build rate directly reduces manufacturing time, corresponding to optimizing productivity. Building rate is determined by (8), where v, h, and t represent speed (mm/s), hatch distance (mm), and layer thickness (mm), respectively.

$$BR = v.h.t \tag{8}$$

The comparison of points 1 and 2, as shown in Fig. 13, indicates that a slight rise in porosity, from 0.4 to 0.9%, results in a 70% enhancement in the build rate. This considerable increase in productivity markedly decreases fabrication time, providing a significant benefit for high-efficiency production operations. This correlation demonstrates that a controlled increase in defect content can result in a significant improvement in build rate, highlighting the importance of process parameters optimization to achieve higher productivity while balancing component quality.

By establishing the predictive relationship between process parameters and relative density (Fig. 13), this study enables estimating the expected defect content before fabrication. This prediction allows for informed decision-making when selecting process parameter combinations, offering a reliable resource for balancing quality and productivity based on specific application requirements. Such an approach not only minimize defect content but also facilitates customized process optimization in broader manufacturing applications, enhancing the applicability of the proposed methodology beyond the current material system.

Furthermore, developing ML models for process parameter optimization involves considerable computational and time expenses. The beginning steps may require considerable resources, including data acquisition, preprocessing, model training, and hyperparameter tuning. Cross-validation and hyperparameter tuning might require significant time and computational resources. Following the completion of training, machine learning models may rapidly predict optimal parameters, decreasing the necessity for substantial physical experiments. The reusability of models across many manufacturing conditions minimizes initial costs, offering ML as an efficient tool for improving productivity and reducing trial-and-error in AM [62].

3.5 Microstructure and hardness

The sample with the highest relative density of 99.9% was chosen for microstructure analysis. Figure 14 illustrates that the SEM backscattered images show the characteristics of AISI316L-Cu. The microstructure includes a mixture of equiaxed and columnar cells, demonstrating a unique grain form produced by the L-PBF process. These figures illustrate the absence of metallurgical defects, such as pores or cracks, especially in the interface region. The solidification of the melt pool in the AISI316L-Cu alloy

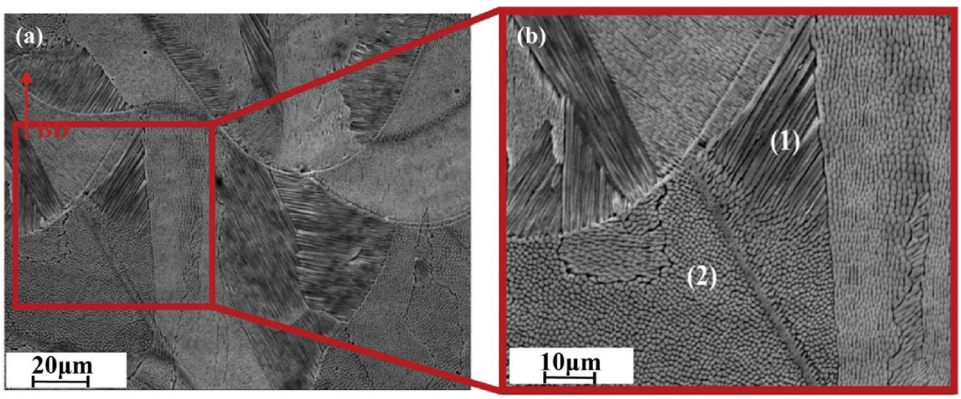


Fig. 14 SEM backscattered images highlighting the microstructure of the optimum sample with 99.9% relative density. **a** depicts the melt pools with clearly defined grain shapes, **b** offers an enlarged perspective, with (1) displaying equiaxed cells and (2) presenting columnar cells

shows the formation of columnar grains with cellular substructures, confirming the higher cooling rates resulting from the L-PBF process [63]. Adding copper optimizes the temperature gradient and cooling rate during solidification. This enhancement can be attributed to the superior thermal conductivity of copper, as previously documented (cooling rate of 1.8×10^6 K/s for AISI316L-Cu compared to 1.1×10^6 K/s for AISI316L) [64]. Adding copper to iron forms a solid solution, with copper providing an austenite stabilizer. This stability enables the development of an utterly austenitic structure, as validated by previous research [65, 66]. These features enhance the mechanical properties of this alloy compared to AISI316L, especially hardness, by increasing grain boundary density and hindering dislocation movement. The hardness of the chosen samples was measured, resulting in a value of 243 HV for AISI316L-Cu, which is higher than the 220 HV reported for pure AISI316L fabricated by L-PBF [67]. This improvement is due to the addition of copper, which results in a refined microstructure and enhanced resistance to plastic deformation [66].

Moreover, this study mainly aims to optimize process parameters based on relative density. However, the previous literature highlights the necessity of predicting hardness using ML models in components produced by L-PBF process [68]. Gradient boosting models were developed using important process parameters (laser power, scanning speed, layer thickness, hatch distance, and material density) to predict microhardness. The results show that choosing the optimal process parameters to get the desired mechanical properties is complex and depends on the material used. Machine learning models, such as GBR and GPR, have shown high accuracy ($R^2 > 0.96$) in predicting microhardness based on L-PBF parameters across various alloys [69–72], highlighting that the optimal parameters for density may not necessarily align with those required for maximizing hardness.

4 Conclusion

This study utilized machine learning-based process parameter optimization with seven algorithms (BR, DTR, GBR, GPR, KNN, RFR, and SVR) to establish a relationship between process parameters and porosity content in the L-PBF process. The findings highlight the potential of ML to optimize process parameters, balance productivity with defect minimization, and enhance the engineering applications of the L-PBF process. Moreover, this study demonstrates a trade-off between productivity and porosity. By optimizing the process parameter with the ML framework, this study provides a multi-objective optimization perspective, enabling the identification of parameter combinations that balance high productivity with high relative density. Such an approach can guide engineers in selecting process parameters according to specific priorities in industrial applications. The important conclusions are as follows:

- The analysis demonstrated that laser power, scan speed, and hatch distance significantly influenced the relative density, with optimal combinations achieving densities above 99%.
- Among the algorithms with optimized hyperparameters and different training sizes, the SVR model with a training size of 80% was chosen as the most accurate model, demonstrating the lowest error ($R^2 = 0.842$, MAE = 0.601, and MSE = 0.640). This implies that the built data-driven framework can predict the defect content of samples under different combinations of process parameters for various purposes.
- The optimal process parameters for achieving relative densities above 99% were identified as a 200–250 W laser power, a scan speed of 800 mm/s, and a hatch distance of 0.13 mm.

Table 3 Process parameters for AISI316L-2.5%Cu thereof utilized in the design of experiments

S.ID	Power (W)	Scan speed (mm/s)	Hatch distance (mm)
1	100	1000	0.1
2	100	800	0.1
3	150	1000	0.12
4	190	400	0.1
5	190	600	0.1
6	190	800	0.1
7	190	1000	0.1
8	200	400	0.1
9	200	600	0.1
10	200	800	0.1
11	200	1000	0.1
12	270	400	0.1
13	270	600	0.1
14	270	800	0.1
15	270	1000	0.1
16	340	400	0.1
17	340	600	0.1
18	340	800	0.1
19	340	1000	0.1
20	190	400	0.11
21	190	600	0.11
22	190	800	0.11
23	190	1000	0.11
24	200	400	0.11
25	200	600	0.11
26	200	800	0.11
27	200	1000	0.11
28	270	400	0.11
29	270	600	0.11
30	270	800	0.11
31	270	1000	0.11
32	340	400	0.11
33	340	600	0.11
34	340	800	0.11
35	340	1000	0.11
36	190	400	0.12
37	190	600	0.12
38	190	800	0.12
39	190	1000	0.12
40	200	400	0.12
41	200	600	0.12
42	200	800	0.12
43	200	1000	0.12
44	200	1000	0.2
45	200	800	0.2
46	270	400	0.12
47	270	600	0.12
48	270	800	0.12
49	270	1000	0.12
50	340	400	0.12
51	340	600	0.12
52	340	800	0.12
53	340	1000	0.12
54	190	400	0.13
55	190	600	0.13

Table 3 (continued)

S.ID	Power (W)	Scan speed (mm/s)	Hatch distance (mm)
56	190	800	0.13
57	190	1000	0.13
58	190	1000	0.13
59	200	400	0.13
60	200	600	0.13
61	200	800	0.13
62	200	1000	0.13
63	270	400	0.13
64	270	600	0.13
65	270	800	0.13
66	270	1000	0.13
67	270	1000	0.2
68	340	400	0.13
69	340	600	0.13
70	340	800	0.13
71	340	1000	0.13

Appendix: Table of process parameters used in the design of experiments

See Table 3.

Author contributions A.S. and A.B.: Conceptualization A.M., S.T, M.T. and A.B.: Design the experiments, Print the samples, Analyze the samples A.M. and S.T.: Collect the data, prepare figures, and write the first draft A.B., M.T., A.S. and L.I.: Review the papaer A.S. and L.I.: Project admistration and resources.

Funding Open access funding provided by Politecnico di Torino within the CRUI-CARE Agreement.

Data availability No datasets were generated or analysed during the current study.

Declarations

Competing interests The authors declare no competing interests.

Open Access This article is licensed under a Creative Commons Attribution 4.0 International License, which permits use, sharing, adaptation, distribution and reproduction in any medium or format, as long as you give appropriate credit to the original author(s) and the source, provide a link to the Creative Commons licence, and indicate if changes were made. The images or other third party material in this article are included in the article's Creative Commons licence, unless indicated otherwise in a credit line to the material. If material is not included in the article's Creative Commons licence and your intended use is not permitted by statutory regulation or exceeds the permitted use, you will need to obtain permission directly from the copyright holder. To view a copy of this licence, visit http://creativecommons.org/licenses/by/4.0/.

References

1. Saboori A, Aversa A, Marchese G et al (2019) Application of directed energy deposition-based additive manufacturing in repair. Appl Sci. https://doi.org/10.3390/app9163316
2. Ghanavati R, Naffakh-Moosavy H, Moradi M et al (2023) Residual stresses and distortion in additively-manufactured SS316L-IN718 multi-material by laser-directed energy deposition: a validated numerical-statistical approach. J Manuf Process 108:292–309. https://doi.org/10.1016/j.jmapro.2023.11.018
3. Rinaldi M, Ghidini T, Cecchini F et al (2018) Additive layer manufacturing of poly (ether ether ketone) via FDM. Compos Part B Eng 145:162–172
4. Mosallanejad MH, Niroumand B, Aversa A, Saboori A (2021) In-situ alloying in laser-based additive manufacturing processes: a critical review. J Alloys Compd 872:159567. https://doi.org/10.1016/j.jallcom.2021.159567
5. Saboori A, Toushekhah M, Aversa A et al (2020) Critical features in the microstructural analysis of AISI 316L produced by metal additive manufacturing. Metallogr Microstruct Anal 9:92–96. https://doi.org/10.1007/s13632-019-00604-6
6. Dadkhah M, Tulliani J-M, Saboori A, Iuliano L (2023) Additive manufacturing of ceramics: advances, challenges, and outlook. J Eur Ceram Soc 43:6635–6664. https://doi.org/10.1016/j.jeurceramsoc.2023.07.033
7. Liu K, Wu T, Bourell DL et al (2018) Laser additive manufacturing and homogeneous densification of complicated shape SiC ceramic parts. Ceram Int 44:21067–21075. https://doi.org/10.1016/j.ceramint.2018.08.143
8. behjat A, Saboori A, Galati M, Iuliano L (2024) The electrochemical behaviour of Ti-48Al-2Cr-2Nb produced by electron beam powder bed fusion process. Intermetallics 175:108472. https://doi.org/10.1016/j.intermet.2024.108472
9. Aiza I, Baldi C, de la Vega FM et al (2025) Effects of build orientation and inclined features on physical, microstructural and mechanical properties of powder bed fusion additively manufactured metallic parts. Prog Mater Sci 147:101357. https://doi.org/10.1016/j.pmatsci.2024.101357
10. Liu K, Gu D, Guo M, Sun J (2022) Effects of processing parameters on densification behavior, microstructure evolution and mechanical properties of W-Ti alloy fabricated by laser powder bed fusion. Mater Sci Eng A 829:142177

11. Calignano F (2018) Investigation of the accuracy and roughness in the laser powder bed fusion process. Virtual Phys Prototyp 13:97–104
12. Eliasu A, Duntu SH, Hukpati KS et al (2022) Effect of individual printing parameters on residual stress and tribological behaviour of 316L stainless steel fabricated with laser powder bed fusion (L-PBF). Int J Adv Manuf Technol 119:7041–7061
13. Milewski JO (2017) Additive manufacturing of metals: from fundamental technology to rocket nozzles, medical implants, and custom jewelry. Addit Manuf Met
14. Zhang M, Liu C, Shi X et al (2016) Residual stress, defects and grain morphology of Ti-6Al-4V alloy produced by ultrasonic impact treatment assisted selective laser melting. Appl Sci 6:304. https://doi.org/10.3390/app6110304
15. Ansarian I, Taghiabadi R, Amini S et al (2024) Improvement of surface mechanical and tribological characteristics of L-PBF processed commercially pure titanium through ultrasonic impact treatment. Acta Metallurgica Sinica (English Letters) 37:1034–1046. https://doi.org/10.1007/s40195-024-01696-y
16. Patel S, Vlasea M (2020) Melting modes in laser powder bed fusion. Materialia 9:100591
17. Oliveira JP, LaLonde AD, Ma J (2020) Processing parameters in laser powder bed fusion metal additive manufacturing. Mater Des 193:108762
18. Marrey M, Malekipour E, El-Mounayri H, Faierson EJ (2019) A framework for optimizing process parameters in powder bed fusion (PBF) process using artificial neural network (ANN). Procedia Manuf 34:505–515. https://doi.org/10.1016/j.promfg.2019.06.214
19. Behjat A, Shamanian M, Sadeghi F et al (2025) Process-driven structural and property evolution in laser powder bed fusion of a newly developed AISI 316L stainless steel. Materials 18:3343. https://doi.org/10.3390/ma18143343
20. Pham D-P, Tran H-C (2025) Optimization of in-situ laser remelting parameters for enhancing mechanical properties of parts produced by laser powder bed fusion process. Opt Laser Technol 181:111636
21. Calignano F, Minetola P (2019) Influence of process parameters on the porosity, accuracy, roughness, and support structures of hastelloy X produced by laser powder bed fusion. Materials (Basel) 12:1–10. https://doi.org/10.3390/ma12193178
22. Chen L, Richter B, Zhang X et al (2020) Modification of surface characteristics and electrochemical corrosion behavior of laser powder bed fused stainless-steel 316L after laser polishing. Addit Manuf 32:101013. https://doi.org/10.1016/j.addma.2019.101013
23. Marchese G, Parizia S, Saboori A et al (2020) The influence of the process parameters on the densification and microstructure development of laser powder bed fused Inconel 939. Metals. https://doi.org/10.3390/met10070882
24. Zhang Z, Chu B, Wang L, Lu Z (2019) Comprehensive effects of placement orientation and scanning angle on mechanical properties and behavior of 316L stainless steel based on the selective laser melting process. J Alloys Compd 791:166–175
25. Ziri S, Hor A, Mabru C (2022) Combined effect of powder properties and process parameters on the density of 316L stainless steel obtained by laser powder bed fusion. Int J Adv Manuf Technol 120:6187–6204
26. Liu Q, Wu H, Paul MJ et al (2020) Machine-learning assisted laser powder bed fusion process optimization for AlSi10Mg: new microstructure description indices and fracture mechanisms. Acta Mater 201:316–328
27. Tapia G, Elwany AH, Sang H (2016) Prediction of porosity in metal-based additive manufacturing using spatial Gaussian process models. Addit Manuf 12:282–290
28. Silbernagel C, Aremu A, Ashcroft I (2019) Using machine learning to aid in the parameter optimisation process for metal-based additive manufacturing
29. Abele E, Stoffregen HA, Kniepkamp M et al (2015) Selective laser melting for manufacturing of thin-walled porous elements. J Mater Process Technol 215:114–122. https://doi.org/10.1016/j.jmatprotec.2014.07.017
30. Moradi A, Tajalli S, Mosallanejad MH, Saboori A (2024) Intelligent laser - based metal additive manufacturing : A review on machine learning for process optimization and property prediction. Springer, London
31. Rankouhi B, Jahani S, Pfefferkorn FE, Thoma DJ (2021) Compositional grading of a 316L-Cu multi-material part using machine learning for the determination of selective laser melting process parameters. Addit Manuf 38:101836. https://doi.org/10.1016/j.addma.2021.101836
32. Gu Z, Sharma S, Riley DA et al (2023) A universal predictor-based machine learning model for optimal process maps in laser powder bed fusion process. J Intell Manuf 34:3341–3363
33. Barik S, Bhandari R, Mondal MK (2024) Optimization of wire arc additive manufacturing process parameters for low-carbon steel and properties prediction by support vector regression model. Steel Res Int 95:2300369
34. Chung H-T, Tsai C-C, Jen K-K et al (2024) Optimization of process parameters of selective laser melted nickel-based superalloy for densification by random forest regression algorithm and response surface methodology. Results Eng 22:102182. https://doi.org/10.1016/j.rineng.2024.102182
35. Gor M, Dobriyal A, Wankhede V et al (2022) Density prediction in powder bed fusion additive manufacturing: machine learning-based techniques. Appl Sci 12:7271
36. Lee SH (2020) Optimization of cold metal transfer-based wire arc additive manufacturing processes using gaussian process regression. Metals (Basel) 10:461
37. Zhu X, Jiang F, Guo C et al (2023) Prediction of melt pool shape in additive manufacturing based on machine learning methods. Opt Laser Technol. https://doi.org/10.1016/j.optlastec.2022.108964
38. Akbari P, Zamani M, Mostafaei A (2024) Machine learning prediction of mechanical properties in metal additive manufacturing. Addit Manuf 91:104320. https://doi.org/10.1016/j.addma.2024.104320
39. Chepiga T, Zhilyaev P, Ryabov A et al (2023) Process parameter selection for production of stainless steel 316L using efficient multi-objective Bayesian optimization algorithm. Materials (Basel) 16:1050
40. Duchi J (2017) CS229 Supplemental Lecture notes Hoeffding's inequality
41. Chinchanikar S, Shaikh AA (2022) A review on machine learning, big data analytics, and design for additive manufacturing for aerospace applications. J Mater Eng Perform 31:6112–6130. https://doi.org/10.1007/s11665-022-07125-4
42. Behjat A, Shamanian M, Sadeghi F et al (2024) Additive manufacturing of a novel in-situ alloyed AISI316L-Cu stainless steel: microstructure and antibacterial properties. Mater Lett 355:135363. https://doi.org/10.1016/j.matlet.2023.135363
43. Xi T, Shahzad MB, Xu D et al (2017) Effect of copper addition on mechanical properties, corrosion resistance and antibacterial property of 316L stainless steel. Mater Sci Eng C 71:1079–1085. https://doi.org/10.1016/j.msec.2016.11.022
44. Behjat A, Shamanian M, Iuliano L, Saboori A (2024) Laser powder bed fusion in situ alloying of AISI 316L-2.5%Cu alloy: microstructure and mechanical properties evolution. Prog Addit Manuf. https://doi.org/10.1007/s40964-023-00557-x
45. Ara I, Azarmi F, Tangpong XW (2021) Microstructure analysis of high-density 316L stainless steel manufactured by selective laser

melting process. Metallogr Microstruct Anal 10:754–767. https://doi.org/10.1007/s13632-021-00798-8
46. Bai S, Perevoshchikova N, Sha Y, Wu X (2019) The effects of selective laser melting process parameters on relative density of the AlSi10Mg parts and suitable procedures of the archimedes method. Appl Sci 9:583
47. Yan F, Lin Z, Wang X et al (2017) Evaluation and prediction of bond strength of GFRP-bar reinforced concrete using artificial neural network optimized with genetic algorithm. Compos Struct 161:441–452
48. Shen T, Zhang W, Li B (2023) Machine learning-enabled predictions of as-built relative density and high-cycle fatigue life of Ti6Al4V alloy additively manufactured by laser powder bed fusion. Mater Today Commun 37:107286
49. Saboori A, Abdi A, Fatemi SA et al (2020) Hot deformation behavior and flow stress modeling of Ti–6Al–4V alloy produced via electron beam melting additive manufacturing technology in single β-phase field. Mater Sci Eng A 792:139822. https://doi.org/10.1016/j.msea.2020.139822
50. Eshkabilov S, Ara I, Azarmi F (2022) A comprehensive investigation on application of machine learning for optimization of process parameters of laser powder bed fusion-processed 316L stainless steel. Int J Adv Manuf Technol 123:2733–2756. https://doi.org/10.1007/s00170-022-10331-y
51. Chandra M, Vimal KEK, Rajak S (2023) A comparative study of machine learning algorithms in the prediction of bead geometry in wire-arc additive manufacturing. Int J Interact Des Manuf. https://doi.org/10.1007/s12008-023-01326-4
52. Barrionuevo GO, Ramos-Grez JA, Walczak M, Betancourt CA (2021) Comparative evaluation of supervised machine learning algorithms in the prediction of the relative density of 316L stainless steel fabricated by selective laser melting. Int J Adv Manuf Technol 113:419–433
53. Das S (2003) Physical aspects of process control in selective laser sintering of metals. Adv Eng Mater 5:701–711. https://doi.org/10.1002/adem.200310099
54. Liu Q, Elambasseril J, Sun S et al (2014) The effect of manufacturing defects on the fatigue behaviour of Ti-6Al-4V specimens fabricated using selective laser melting. Adv Mater Res 891:1519–1524. https://doi.org/10.4028/www.scientific.net/AMR.891-892.1519
55. Gong H, Rafi K, Gu H et al (2014) Analysis of defect generation in Ti-6Al-4V parts made using powder bed fusion additive manufacturing processes. Addit Manuf. https://doi.org/10.1016/j.addma.2014.08.002
56. Song B, Dong S, Liu Q et al (2014) Vacuum heat treatment of iron parts produced by selective laser melting: microstructure, residual stress and tensile behavior. Mater Des 54:727–733. https://doi.org/10.1016/j.matdes.2013.08.085
57. Gu D, Shen Y (2009) Balling phenomena in direct laser sintering of stainless steel powder: metallurgical mechanisms and control methods. Mater Des 30:2903–2910. https://doi.org/10.1016/j.matdes.2009.01.013
58. Nguyen DS, Park HS, Lee CM (2020) Optimization of selective laser melting process parameters for Ti-6Al-4V alloy manufacturing using deep learning. J Manuf Process 55:230–235. https://doi.org/10.1016/j.jmapro.2020.04.014
59. Gerner D, Azarmi F, McDonnell M, Okeke U (2024) Application of machine learning for optimization of HVOF process parameters. J Therm Spray Technol 33:504–514. https://doi.org/10.1007/s11666-023-01682-3
60. Theeda S, Jagdale SH, Ravichander BB, Kumar G (2023) Optimization of process parameters in laser powder bed fusion of SS 316L parts using artificial neural networks. Metals (Basel). https://doi.org/10.3390/met130508426
61. Kreitcberg A, Brailovski V, Prokoshkin S (2018) New biocompatible near-beta Ti-Zr-Nb alloy processed by laser powder bed fusion: process optimization. J Mater Process Technol 252:821–829. https://doi.org/10.1016/j.jmatprotec.2017.10.052
62. Qin J, Hu F, Liu Y et al (2022) Research and application of machine learning for additive manufacturing. Addit Manuf. https://doi.org/10.1016/j.addma.2022.102691
63. Sohrabpoor H, Salarvand V, Lupoi R et al (2021) Microstructural and mechanical evaluation of post-processed SS 316L manufactured by laser-based powder bed fusion. J Mater Res Technol 12:210–220. https://doi.org/10.1016/J.JMRT.2021.02.090
64. Saboori A, Piscopo G, Lai M et al (2020) An investigation on the effect of deposition pattern on the microstructure, mechanical properties and residual stress of 316L produced by Directed Energy Deposition. Mater Sci Eng A 780:139179. https://doi.org/10.1016/j.msea.2020.139179
65. Hong IT, Koo CH (2005) Antibacterial properties, corrosion resistance and mechanical properties of Cu-modified SUS 304 stainless steel. Mater Sci Eng A 393:213–222. https://doi.org/10.1016/j.msea.2004.10.032
66. Liu Y, Yang J, Yang H et al (2021) Cu-bearing 316L stainless steel coatings produced by laser melting deposition: microstructure and corrosion behavior in simulated body fluids. Surf Coat Technol 428:127868. https://doi.org/10.1016/j.surfcoat.2021.127868
67. Bakhtiarian M, Omidvar H, Mashhuriazar A et al (2024) The effects of SLM process parameters on the relative density and hardness of austenitic stainless steel 316L. J Mater Res Technol 29:1616–1629. https://doi.org/10.1016/j.jmrt.2024.01.237
68. Barrionuevo GO, Walczak M, Ramos-Grez J, Sánchez-Sánchez X (2023) Microhardness and wear resistance in materials manufactured by laser powder bed fusion: machine learning approach for property prediction. CIRP J Manuf Sci Technol 43:106–114. https://doi.org/10.1016/j.cirpj.2023.03.002
69. Li H, Ramezani M, Li M et al (2018) Tribological performance of selective laser melted 316L stainless steel. Tribol Int 128:121–129. https://doi.org/10.1016/j.triboint.2018.07.021
70. AlMangour B, Grzesiak D, Yang J-M (2017) In-situ formation of novel TiC-particle-reinforced 316L stainless steel bulk-form composites by selective laser melting. J Alloys Compd 706:409–418. https://doi.org/10.1016/j.jallcom.2017.01.149
71. Saeidi K, Alvi S, Lofaj F et al (2019) Advanced mechanical strength in post heat treated SLM 2507 at room and high temperature promoted by hard/ductile sigma precipitates. Metals. https://doi.org/10.3390/met9020199
72. Yan X, Gao S, Chang C et al (2020) Microstructure and tribological property of selective laser melted Fe-Mn-Al-C alloy. Mater Lett 270:127699. https://doi.org/10.1016/j.matlet.2020.127699

Publisher's Note Springer Nature remains neutral with regard to jurisdictional claims in published maps and institutional affiliations.